Supporting information

Solid-liquid interface reassembly enhances surface piezoelectric properties: transitioning parallel interface O-MoS_2 to spherical interface ZnS@O-MoS_2

Ting Li[1,2,#], Wenjin Hu[1,#], Changxin Tang[1], Longlong Shu[1]*, Fei Li[3]*

[1]School of Physics and Materials Science, Nanchang University, Nanchang 330031, People's Republic of China
[2]School of Physics and Electronic Information, Nanchang Normal University, Nanchang 330032, People's Republic of China
[3]Electronic Materials Research Laboratory (Key Lab of Education Ministry), State Key Laboratory for Mechanical Behavior of Materials and School of Electronic and Information Engineering, Xi'an Jiaotong University, Xi'an 710049, People's Republic of China

#These authors contributed equally to this work
*Corresponding email: llshu@ncu.edu.cn (L. Shu), ful5@xjtu.edu.cn (F. Li)

Equations (1-11) present the Gibbs free energy change (ΔG) and intermediate species reaction models for the piezo-electrocatalytic CO_2 reduction reaction in parallel interface O-MoS_2 and spherical interface ZnS@O-MoS_2. The entire piezo-electrocatalytic CO_2 reduction reaction pathway corresponds to labeled reaction steps (1-8), where the change in free energy is determined by subtracting the Gibbs free energy of the reactants from that of the products, as specified in equations (9-11). Under isothermal and isobaric conditions, a reaction is spontaneous only if the Gibbs free energy change (ΔG) is negative. The smaller the ΔG, the more readily the CO_2 reduction reaction occurs.

$$CO_2(g) + * \rightarrow *CO_2 \quad (1)$$

$$*CO_2 + H^+ + e^- \rightarrow *COOH \quad (2)$$

$$*COOH + e^- + H^+ \rightarrow *CO + H_2O \quad (3)$$

$$*CO \rightarrow * + CO(g) \quad (4)$$

$$*CO + 4H^+ + 4e^- \rightarrow *CH_3OH \quad (5)$$

$$*CH_3OH + H^+ + e^- \rightarrow *CH_3 + H_2O \quad (6)$$

$$*CH_3 + H^+ + e^- \rightarrow *CH_4 \quad (7)$$

$$^{*}CH_4 \rightarrow {}^{*} + CH_4(g) \tag{8}$$

$$\Delta G[^{*}CO_2] = G[^{*}CO_2] - (G[^{*}] + G[CO_2]) \tag{9}$$

$$\Delta G[^{*}COOH] = G[^{*}COOH] - (G[^{*}] + G[CO_2] + G[H^{+} + e^{-}]) \tag{10}$$

$$\Delta G[^{*}CO] = G[^{*}CO] + G[H_2O] - (G[^{*}] + G[CO_2] + 2 \times G[H^{+} + e^{-}]) \tag{11}$$

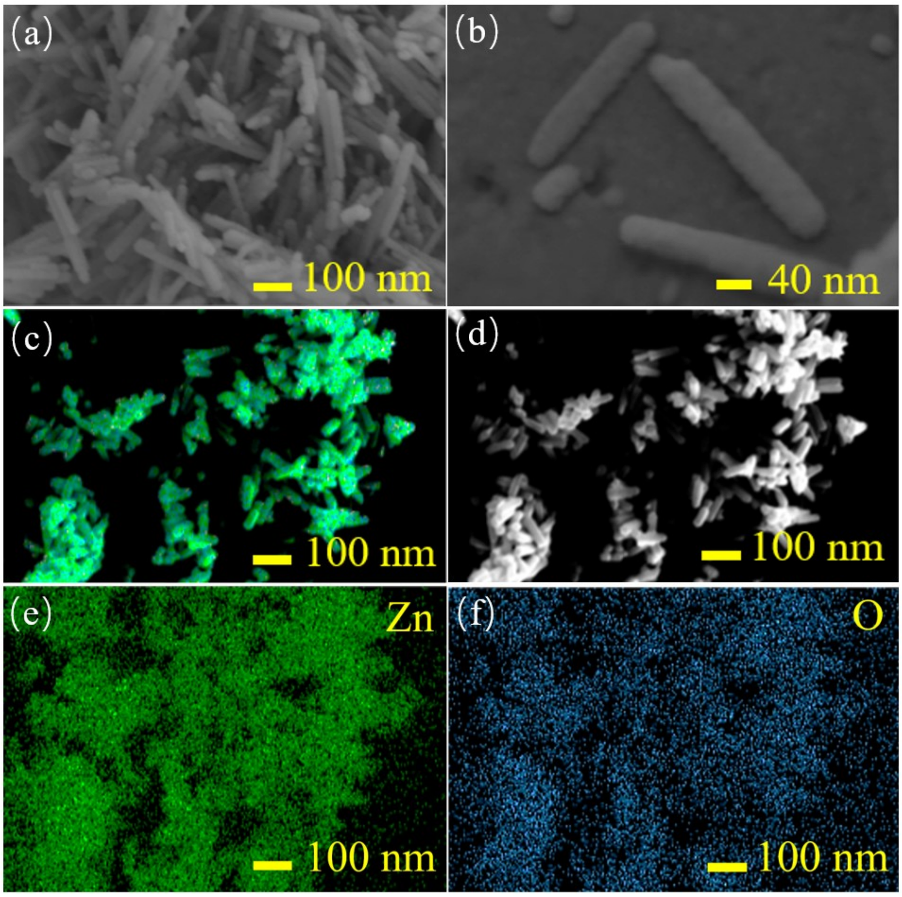

Figure S1. The Scanning Electron Microscopy (SEM) images and Energy Dispersive Spectroscopy (EDS) mapping of Zinc Oxide (ZnO) Nanorods.

Figure S1 (a, b) shows the scanning electron microscopy (SEM) images of the zinc oxide (ZnO) nanorods. The images reveal that ZnO nanorods exhibit a uniform and ordered morphology, with a diameter of around 40 nm and a length of approximately 100 nm. Figure S1 (c) is an EDS mapping overlaid on the SEM image, while Figure S1 (d) displays the SEM image alone, illustrating the morphology and arrangement of the nanorods. Figure S1 (e) and Figure S1 (f) are distribution maps for the Zn element and O element, respectively. Figure S1 (e) shows the uniform and dense distribution of Zn, while Figure S1 (f) demonstrates the distribution of the O element. The comparison between these two images further confirms that the sample is indeed ZnO nanorods. This set of images comprehensively showcases the morphological characteristics, elemental composition, and distribution of the ZnO nanorods, indicating the uniformity and consistency of the sample.

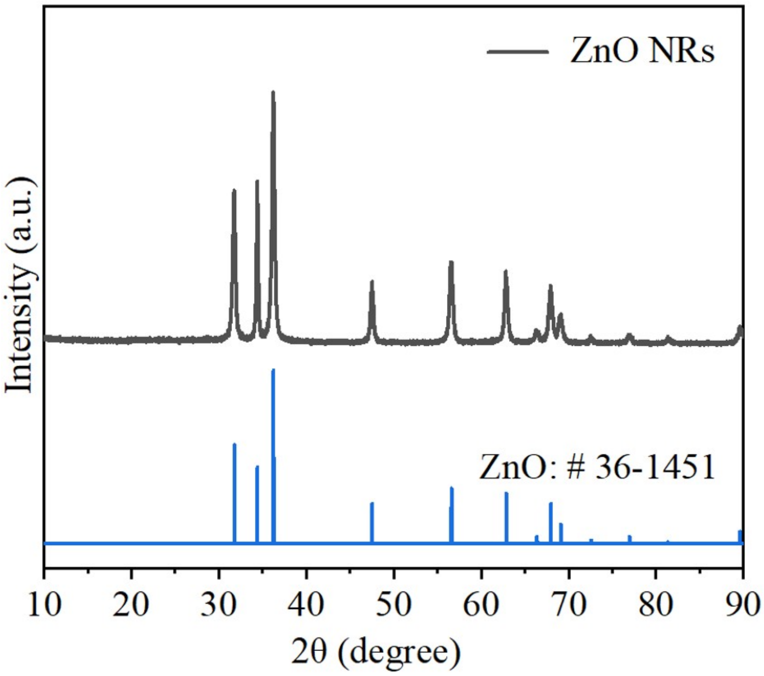

Figure S2. The X-ray diffraction (XRD) pattern of the synthesized zinc oxide (ZnO) nanorods.

Figure S2 shows the X-ray diffraction (XRD) pattern of the synthesized zinc oxide (ZnO) nanorods. By comparing the black experimental data curve with the standard reference data (JCPDS card No. 36-1451), the synthesized material can be clearly confirmed as ZnO nanorods. The diffraction peaks in the pattern closely match the standard diffraction peaks of ZnO, indicating that the synthesized material is pure hexagonal wurtzite structured ZnO with high crystallinity. The main diffraction peaks appear at 2θ positions of 31.7°, 34.4°, 36.2°, 47.5°, 56.6°, 62.8°, and 68.0°, corresponding to the standard ZnO crystal planes, consistent with the JCPDS database. This confirms that the synthesis method effectively prepared ZnO nanorods with good crystal structure and high purity.

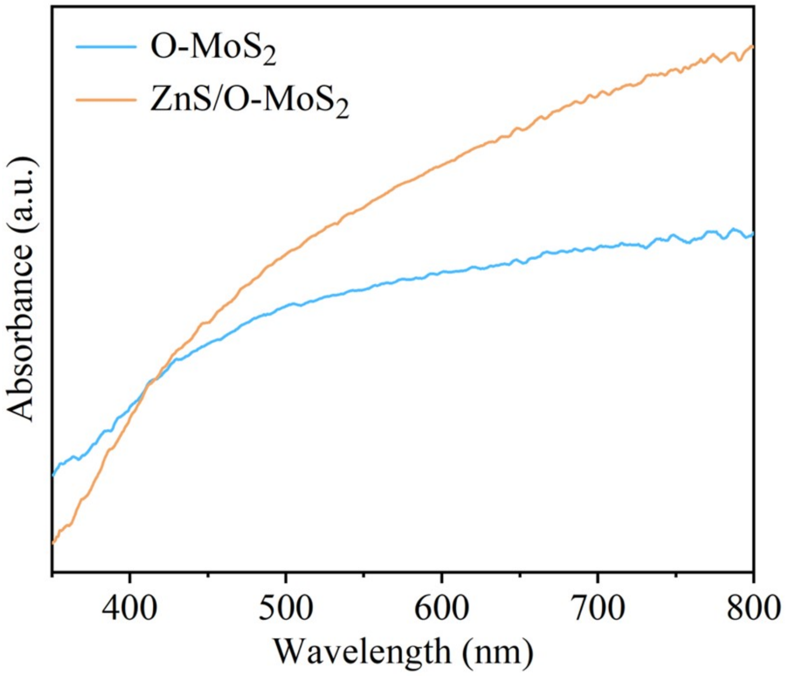

Figure S3. The Ultraviolet–visible (UV-Vis) absorption spectra of O-MoS_2 and ZnS@O-MoS_2.

Figure S3 presents the UV-Vis absorption spectra of O-MoS_2 and ZnS/O-MoS_2. The spectra reveal that the absorption spectrum of O-MoS_2 (blue curve) steadily rises with wavelength between 400 nm and 800 nm, whereas the ZnS/O-MoS_2 (orange curve) demonstrates much higher absorbance from 416 nm to 800 nm, particularly beyond 600 nm. This indicates that the light absorption performance of ZnS/O-MoS_2 is significantly enhanced in the visible to near-infrared region (500 nm to 800 nm), which is speculated to be related to changes in the band structure or interface states caused by the introduction of ZnS.

The band gap width can be determined using the UV-Vis spectrophotometric method, where the UV-Vis absorption spectrum has the x-axis representing wavelength and the y-axis representing absorbance. The band gap width determined through the spectrophotometric method is referred to as the optical band gap. The widely used Tauc plot method estimates the band gap width of semiconductors utilizing the formula proposed by Tauc, Davis, and Mott:

$$(\alpha h\vartheta)^{1/n} = A(h\vartheta - E_g)$$

where α represents the absorption coefficient (derived from the UV-Vis absorbance), h stands for Planck's constant, ν denotes the frequency of light (calculated from the wavelength), A is a constant, and Eg is the semiconductor band gap; n varies according to the type of semiconductor, where n=2 for indirect band gap semiconductors and n=1/2 for direct band gap semiconductors.

Table S1. Electrochemical data and charge carrier properties of O-MoS_2 and ZnS@O-MoS_2.

Materials	R_d (Ω)	R_{ct} (Ω)	C_μ (F)	L (cm)	τ_n (s)	D_n ($cm^2 \cdot s^{-1}$)	L_n (cm)
O-MoS_2	6.02 E+06	4.52	0. 011	0.03	0.05	1.33 E-08	2.60 E-05
ZnS@ O-MoS_2	6.64 E+06	61.58	0.004	0.03	0.24	3.46 E-08	9.14 E-05

The carrier transport properties are listed in Table S1. The high-frequency arc represents the diffusion resistance (R_d) of charge transfer along the catalyst interface. The mid-frequency arc represents the charge transfer resistance (R_{ct}) at the catalyst interface, where C_μ is the chemical capacitance and L is the thickness of the working electrode. The values of R_d, R_{ct}, and C_μ were analyzed using the complex-nonlinear least-squares (CNLS) fitting method in the ZView 3.1 software. Carrier transport properties, such as electron lifetime (t_n), electron diffusion coefficient (D_n), and effective diffusion length (L_n), can be calculated using the following formulas:

$$\tau_n = R_{ct}C_\mu,\ D_n = L^2/R_dC_\mu,\ \ L_n = (\tau_n D_n)^{1/2}$$